AGU
ADVANCING EARTH AND SPACE SCIENCES

Geophysical Research Letters®

Key Points:

- We have identified high-scattering basal ice in Jutulstraumen Glacier's onset region using radar, reaching several hundred meters from the bed
- Backscatter analysis suggests that the basal ice units contain unstratified point scatters and cause little radio-glaciological loss
- 3D thermo-mechanical modeling implies that freeze-on of basal meltwater generated upstream likely initially formed the basal ice units

Correspondence to:

S. Franke,
steven.franke@uni-tuebingen.de;
steven.franke@posteo.de

Sediment Freeze-On and Transport Near the Onset of a Fast-Flowing Glacier in East Antarctica

Steven Franke[1] ⓘ**, Michael Wolovick[2]** ⓘ**, Reinhard Drews[1]** ⓘ**, Daniela Jansen[2]** ⓘ**, Kenichi Matsuoka[3]** ⓘ**, and Paul D. Bons[1,4]** ⓘ

[1]Department of Geosciences, Tübingen University, Tübingen, Germany, [2]Alfred Wegener Institute, Helmholtz Centre for Polar and Marine Research, Bremerhaven, Germany, [3]Norwegian Polar Institute, Tromsø, Norway, [4]China University of Geosciences (Beijing), Beijing, PR China

Abstract Understanding the material properties and physical conditions of basal ice is crucial for a comprehensive understanding of Antarctic ice-sheet dynamics. Yet, direct data are sparse and difficult to acquire. Here, we employ ultra-wideband radar to map high-backscatter zones near the glacier bed within East Antarctica's Jutulstraumen drainage basin. Our backscatter analysis reveals that the basal ice in an area of ~10,000 km^2 is composed of along-flow oriented sediment-laden basal ice units connected to the basal substrate, extending up to several hundred meters thick. Three-dimensional thermomechanical modeling supports that these units form via basal freeze-on of subglacial water that originated from further upstream. Our findings suggest that basal freeze-on, and the entrainment and transport of subglacial material play a significant role in an accurate representation of material, physical, and rheological properties of the Antarctic ice sheet's basal ice, ultimately enhancing the accuracy and reliability of ice-sheet modeling.

Plain Language Summary We investigate the lowermost portion of the ice column of the Antarctic ice sheet, known as basal ice. This part holds crucial information about how the ice sheet behaves when it flows. Using the principle of echo-location, we use radar technology to scan the ice in East Antarctica's Jutulstraumen drainage basin. We discover that a significant portion of the basal ice in this region is filled with sediment and can be several hundred meters thick. To better understand how this distinctive type of ice forms, we used a mathematical model that suggested that these ice units likely form when water underneath the ice is transported and refreezes at particular locations. Our findings highlight the importance of these freezing and mixing of materials from beneath the ice. Understanding where these ice units are located provides important information for ice-flow models to ultimately better understand how the Antarctic ice sheet behaves in the future.

1. Background

The future of the Antarctic ice sheet (AIS) significantly depends on its dynamic behavior with ongoing global warming (Garbe et al., 2020; Stokes et al., 2022). While surface processes of the AIS are relatively convenient to study, the processes at the ice base remain challenging to investigate due to their inaccessibility. However, a better understanding of the physical conditions, material properties, and mechanical processes at the ice-bed interface, such as basal ice temperature, subglacial hydrology, and basal sliding (Dawson et al., 2022; Kazmierczak et al., 2022; Pollard & DeConto, 2012), are critical factors influencing ice-sheet configuration and ice flow (Pattyn, 2010). Airborne geophysical methods like radar give us insight into the englacial and subglacial processes. The focus in this study, lies in the bottom 10%–30% of the AIS (Gades et al., 2000; Robin et al., 1969; Schroeder et al., 2013), although this zone typically lacks clear reflections making it difficult to decipher (Drews et al., 2009; Lilien et al., 2021).

Advancements in radar technology over the last few decades have enabled the detection of subunits within the basal ice layer, previously designated as the echo-free zone, exhibiting distinct units of high-backscatter, reaching thicknesses of several hundred meters (Bell et al., 2011, 2014; Leysinger Vieli et al., 2018; Ross et al., 2020; Wrona et al., 2018). The presence of these distinct zones implies significantly different dielectric properties within these regions compared with the echo-free or low-backscatter zone. Thus far, the differing dielectric properties have been primarily attributed to basal freeze-on and the inclusion of point scatterers, which, in turn, enabled considerations regarding the processes responsible for the formation of these units. These processes encompass phenomena such as freeze-on of subglacial water (Bell et al., 2011; Creyts et al., 2014) and the incorporation of sediments (Kjær et al., 2018; Winter et al., 2019).

Visualization: Steven Franke
Writing – original draft: Steven Franke
Writing – review & editing:
Michael Wolovick, Reinhard Drews,
Daniela Jansen, Kenichi Matsuoka, Paul
D. Bons

Extensive regions of basal freeze-on units, such as those identified beneath the Gamburtsev Subglacial Mountains at Dome A, can impact the rheological properties and fabric structure of the ice column, as well as the continuity of climatic records, making it relevant for ice core drilling projects and ice flow modeling (Bell et al., 2011). This type of basal ice may be prevalent throughout the AIS as initial indications of similar basal ice units have emerged in East Antarctica's western Dronning Maud Land (Franke et al., 2023). Radar forward modeling conducted on prominent ice units in this region has moreover strengthened the hypothesis of embedded point reflectors (Franke et al., 2023). The diffuse character of hyperbolas originating from these basal ice units, repeating but not laminar changes in dielectric properties, as well as low apparent englacial attenuation, point toward entrained englacial sediment with low dielectric properties that could account for the observed high-backscatter reflectivity patterns.

Here, we focus on a spatial analysis of high-backscatter zones (HBZs) detected in the basal ice environment at the onset of Jutulstraumen glacier in East Antarctica using radar data (Figure 1) to investigate their formation and link to the basal thermal conditions. We attribute the reflection pattern of the HBZs to embedded sediment particles in the basal ice. HBZs are several hundred meters thick and widespread in this region. Bed return power analysis suggests that HBZs are radioglaciologically transparent. Furthermore, their spatial distribution follows specific patterns influenced by ice dynamics, englacial basal temperature, and bed topography. We hypothesize that basal freeze-on under specific ice sheet conditions leads to the development of basal ice structures and the concurrent incorporation of sediment. The detection and investigation of sediment-laden basal ice units at an ice-stream onset region offers novel insights into potential formation mechanisms, material properties, and implications on sub-glacial sediment transport processes. Hence, a detailed Antarctic-wide mapping and examination of the characteristics and subglacial conditions contributing to the development of these prominent basal ice units is required to assess their holistic role in the Antarctic ice-sheet system.

2. Study Area, Data, and Methods

2.1. The Jutulstraumen Glacier Onset Region

Our study area ($\sim$350 $\times$ 150 km) is centered at the onset of the Jutulstraumen Glacier, where ice accelerates from 5 to 50 m a^{-1} over $\sim$130 km, located within the Jutulstraumen drainage basin in western Dronning Maud Land, East Antarctica (Figure 1). This region marks the transition from the thick ice sheet of the central plateau to the dynamic convergent ice flow regime leading through the Jutulstraumen Trough, which feeds into the Fimbul Ice Shelf. Our radar profiles are composed of southern and northern blocks, each aligned approximately perpendicular to ice flow and spaced at intervals of 7.5 km. The southern set encompasses a region characterized by deep troughs in the bed topography, indicating a preserved glacial landscape (Franke et al., 2021). The northern set covers mainly a preserved fluvial landscape at elevated topography and with smaller valleys.

2.2. Radar Data Acquisition and Processing

We utilized radar data collected in Austral summer 2018/19 with Alfred Wegener Institutes ultra-wideband (AWI UWB) Multichannel Coherent Radar Depth Sounder (MCoRDS 5), operating with an eight-channel antenna array at a frequency range of 180–210 MHz (Alfred-Wegener-Institut Helmholtz-Zentrum für Polar-und Meeresforschung, 2016; Franke et al., 2021). Our data product for analysis consisted of synthetic aperture radar processed data, with a range resolution of 4.3 m and a trace interval of $\sim$15 m. The survey settings and instruments are described in Rodriguez-Morales et al. (2013), Franke et al. (2021, 2022).

In addition to the UWB data, we used a single profile acquired during the Austral summer season 2016/17 using AWI's pulse-limited radar system (EMR; Electromagnetic Radar System) recording at a frequency of 150 MHz (Nixdorf et al., 1999). The data has a nominal range resolution of $\sim$50 m, and trace spacing of 35 m (Wang et al., 2023). Further details on EMR data acquisition and processing are elaborated upon in Karlsson et al. (2018) and Wang et al. (2023).

2.3. Mapping and Characterization of HBZs in Basal Ice

In our study, we define HBZs as follows: (a) they exhibit pronounced backscatter (elevated return power), clearly above the noise level and distinguishable from echo-free or low backscatter zones (Figures 1d and 1e); (b) they display minimal backscatter variation, lacking stratification or multiple individual reflections; (c) they are found at the ice base directly overlying the bed; and (d) they do not exclusively conform to typical reflection patterns
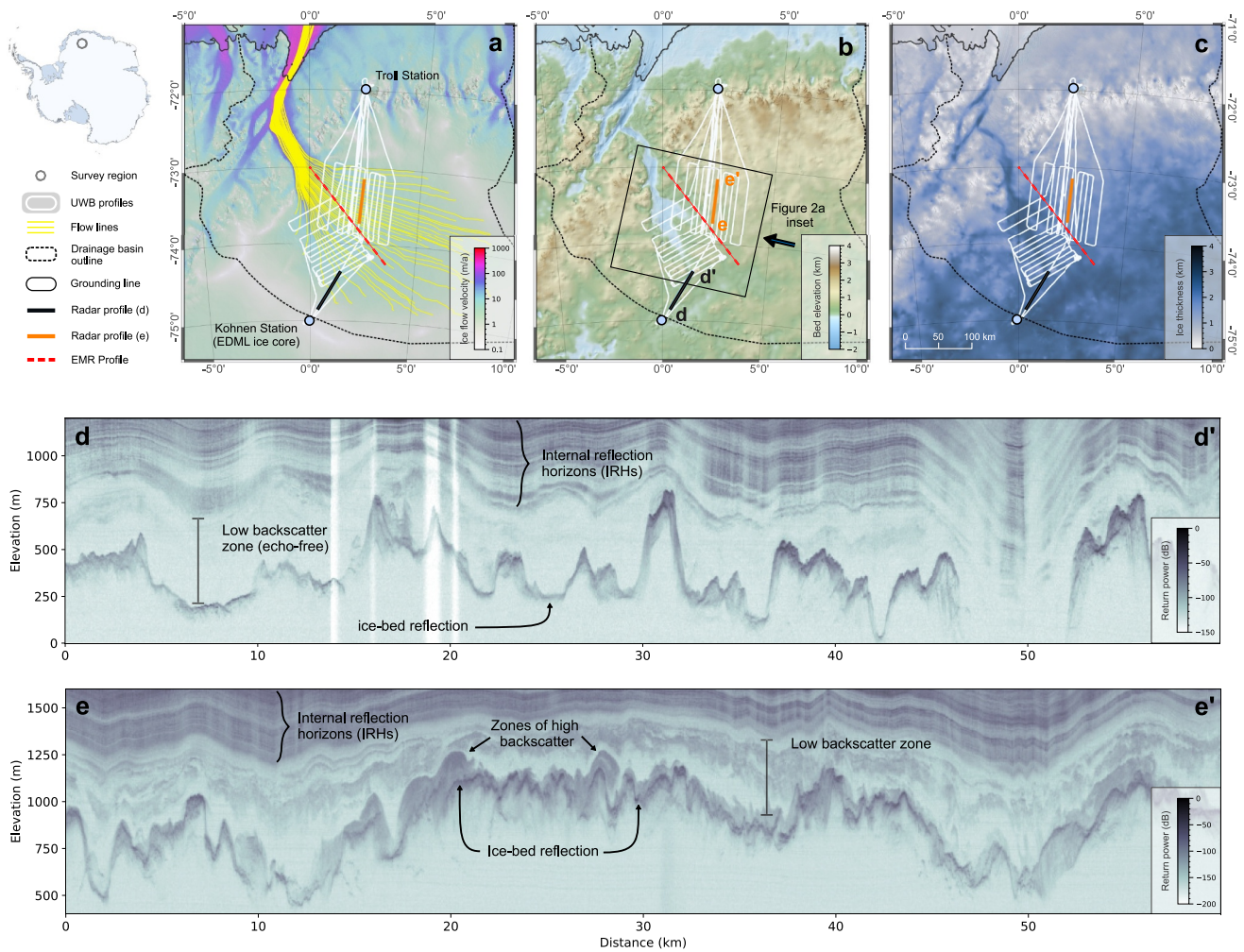
Figure 1. Overview of the study area and radargrams in the Jutulstraumen drainage basin. Panels (a)–(c) show the radar profiles superimposed on ice flow velocity (Mouginot et al., 2019a), bed elevation (Morlighem et al., 2020), and ice thickness (Morlighem et al., 2020). The yellow lines in (a) mark flow trajectories. The black square and arrow in (b) indicate the outline and viewing perspective of the inlet in Figure 2a. Panels (d) and (e) show the near-bed region of two radargrams (lower ~30% of the ice column). Elevation units in (d) and (e) are referenced to the WGS84 ellipsoid, and return power is shown without correcting for geometrical spreading and englacial attenuation.

associated with off-nadir bed reflections. The HBZs were detected by visual assessment, and their outlines were manually traced in the radargrams. To derive the thickness of the HBZs, we determine the two-way travel time difference between the bed reflection and HBZ top. For the conversion from TWT to thickness, we use a dielectric constant of $\varepsilon = 3.15$.

To determine the internal return power of the HBZs and to test whether HBZs significantly attenuate the return power from the bed, we consider three englacial attenuation rates of 10, 20, and 30 dB/km (Matsuoka et al., 2012). We derive the bed return power by following the approach outlined by Jordan et al. (2016) and Oswald and Gogineni (2008) (Text S1 in Supporting Information S1) as it accounts for some of the energy lost by scattering. The same approach is applied to derive the cumulative power of the HBZs (P_{HBZ}), where the power for each pixel through the ice column between the top of the HBZ and bed reflection is summed up. For the consideration of the HBZ return power values in this study, we have excluded those where off-nadir bed reflections potentially overlay the nadir HBZ signal (e.g., Figure 2f).

2.4. Three-Dimensional Thermal Modeling

We use a 3D thermal steady-state model developed by Wolovick et al. (2021), as updated in Kang et al. (2022), to gain insights into basal melting or freezing within our region. This model conserves mass and energy within a
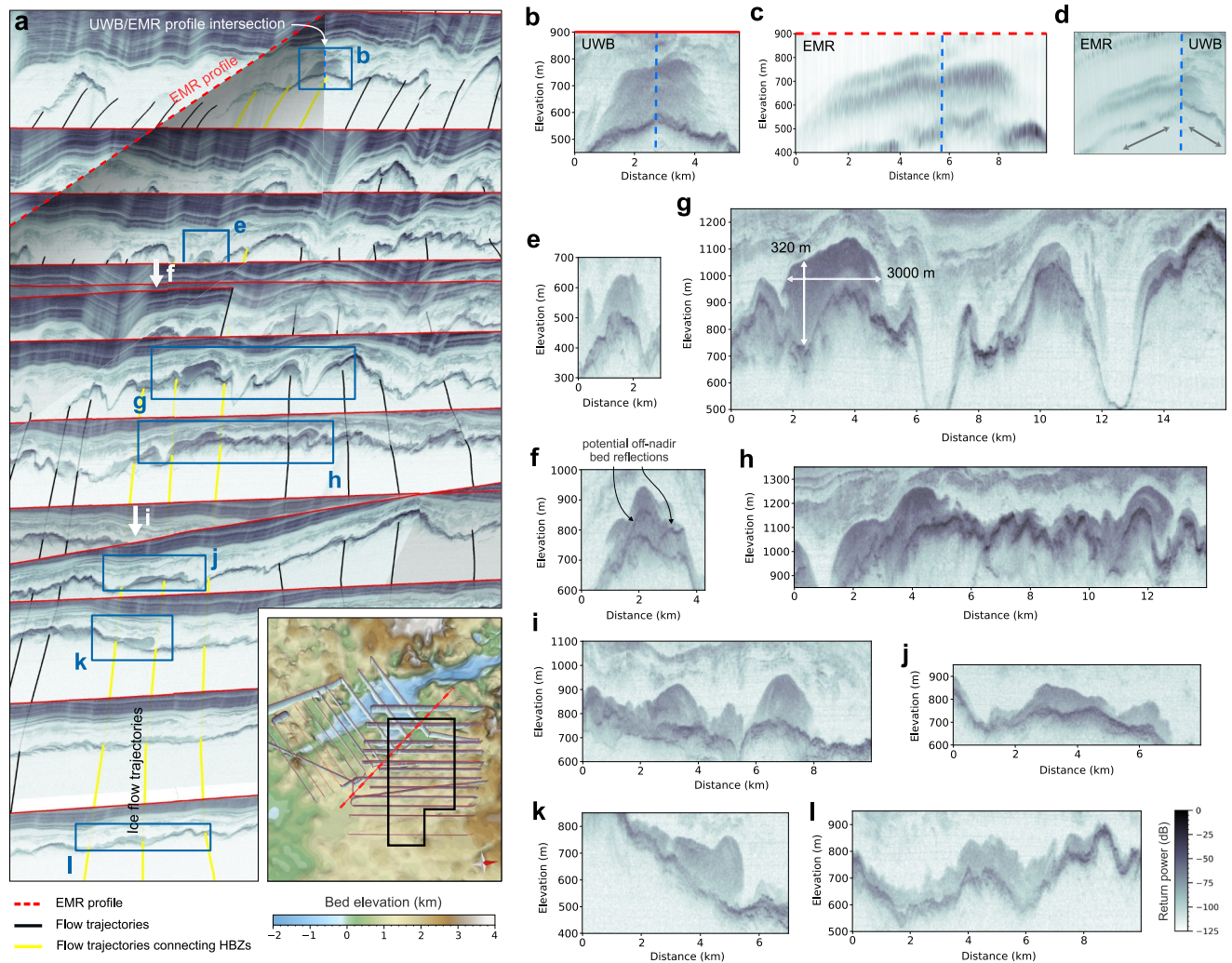
Figure 2. Spatial arrangement and examples of high-backscatter units in the northern set of the JuRaS radar data. The outline of the location of the radar profile is shown in Figure 1c. (a) A three-dimensional (3D) overview of the bottom section of radar profiles (clipped to an elevation of 1,500 m). The black and yellow lines resemble flow trajectories projected to the bed topography (Morlighem et al., 2020). Panels (b)–(l) show magnified parts of the radar profiles in (a). Note that panels (b) and (c) show the same basal unit imaged by the AWI UWB and EMR system, respectively, at different orientations. The profile orientation at this intersection in 3D is shown in (d). Locations of magnified radar views that are covered by a radargram in front of them are marked with a white arrow. Note that all radar data here show UWB data (except for panels (c) and (d), which show EMR data). The dB color bar only applies to UWB data.

coupled, internally consistent solution between the ice-sheet flow field, temperature structure, and basal hydrology. Vertically integrated horizontal ice flux follows a balance flux algorithm with a flow direction field created using a weighted sum of the smoothed surface gradient direction and the direction of observed velocity. Although this is primarily a shallow-ice model, the updates in Kang et al. (2022) were meant to allow the model to achieve reliable temperature solutions in fast-flowing ice streams by incorporating information from surface velocity observations and offline coupling with a Full Stokes mechanical model. We do not employ offline coupling with a mechanical model here, but we do retain the surface velocity observations, which constrain the flow direction field in areas where the ice is flowing fast enough for the observations to be reliable.

Vertically resolved horizontal flow is given by a shape function computed from the temperature-dependent rheology of ice, and basal sliding is computed from the difference between balance velocity and deformation velocity in areas where the basal temperature is close to the melting point. Where basal temperature is cold, the deformation velocity is only used to compute the shape function, which is scaled to match the balance velocity. Vertical ice velocity is computed by integrating the divergence of horizontal velocity up from the bed. Other aspects of the model are as in Wolovick et al. (2021), including subglacial water routing and freeze-on. We force

the model with surface temperatures from Comiso (2000) and accumulation rates from a mean of Arthern et al. (2006) and Berg et al. (2005), with all three data sets accessed through ALBMAP_v1 (Le Brocq et al., 2010). Ice sheet geometry comes from BedMachine Antarctica Version 3 (Morlighem et al., 2020), which has already been updated to include the ice thickness derived from radar data used in this study (Franke et al., 2021).

We examined eight continent-wide geothermal heat flux (GHF) data sets to constrain this model (Figure S3 in Supporting Information S1). The mean and standard deviation GHF of these eight data sets in our model domain is 59 ± 6 mW/m^2. Standard deviations between these models are smaller in the central part of our study area, whereas larger in the northwestern (downstream) and northeastern (partly upstream) regions (Figure S3j in Supporting Information S1). Amongst these eight data sets, we used Martos et al. (2017) as the base data set because it represents a near-mean regional value (64 mW/m^2), and replicates the spatial patterns of upstream melting and freezing in the central part of the study area. We also used GHFs of 5, 10, 15, and 20 mW/m^2 lower than Martos's data set. Moreover, we used regionally uniform GHFs of 50, 55, 60, and 65 mW/m^2 to test whether freeze-on could be produced independent of any particular spatial pattern in GHF.

3. Results

3.1. Spatial Distribution of HBZs

We identify HBZs at the basal ice spanning an approximate total area of ~10,000 km^2, which corresponds to one-third of our study area. They are primarily concentrated within the northern set of radar profiles, and their thickness ranges from a few meters to more than 350 m (Figure 3a). HBZs tend to be flat and with their top surface parallel to the bedrock in the upstream region (Figures 2j and 2l). Further downstream, they become more pronounced and are found concentrated at higher topographic locations. Some discernible HBZs concentrate on mountain summits or transverse slopes (Figures 2f–2h). Furthermore, we observe a trend of increasing HBZ thickness from the upstream to downstream regions (Figure 3a).

In most cases, backscatter within HBZs exhibits slightly monotonically decreasing return power. Sporadic or layer-like reflections, as those shown in Figure 2f, are observed only in a few isolated instances and are most likely an off-nadir bed reflection overlay, which we excluded from the reflectivity analysis. Several prominent HBZs can be traced over several radar profiles and are found to align parallel to the flow direction (yellow flow trajectories in Figure 2a). This alignment suggests that the HBZs observed in these radar profiles form elongated tubes oriented parallel to the ice flow direction. Furthermore, a distinct HBZ is evident at a specific location within the pulse-based EMR data (Figures 2b–2d). At this, the comparison to the UWB profile suggests that: (a) HBZs can be detected with AWI's UWB and EMR system; however, it is evident that the reflection signature in the EMR system is less high-resolution and less sensitive in range; (b) the structure exhibits a three-dimensional character as the profiles are oriented perpendicular to each other; (c) the HBZ reflection pattern is very likely not attributed to off-nadir bed reflections. However, the higher sensitivity with depth of the UWB system makes HBZ detection more likely and shows more details compared to the EMR system.

HBZs predominantly manifest within 1,200–2,400 m of ice thickness and between 200 and 1,500 m of bed elevation (Figure 3d). However, englacial attenuation obscuring the detection of HBZs at greater ice thicknesses renders this boundary somewhat ambiguous. Based on the HBZ mapping from two-dimensional radargrams and considering their horizontal extent and thickness, we derive a mean HBZ thickness of ~90 m and estimate the total volume to be approximately 182 km^3.

3.2. Backscattering Characteristics of HBZs and Ice-Sheet Bed

The evaluation of backscattering characteristics of HBZs and beds with and without HBZs above indicates no systematic influence of HBZs on bed return power (Figure S2a in Supporting Information S1). However, we observe an overall trend of lower to higher HBZ backscatter from the upstream to the downstream region (Figure 3b). This pattern is resembled by different attenuation rates (10, 20, and 30 dB/km; one-way), and appears to be primarily linked to HBZ thickness (Figure S2b in Supporting Information S1), suggesting overall homogeneity in the bulk backscattering characteristics among HBZs. Within the central region, we identified instances of particularly distinct backscattering in certain HBZs (Figures 2g–2j), where the integrated return power of HBZs is significantly higher (5–15 dB) than that of the bed return power (Figure 3c). Notably, these HBZ patches also correlate with high HBZ thickness.
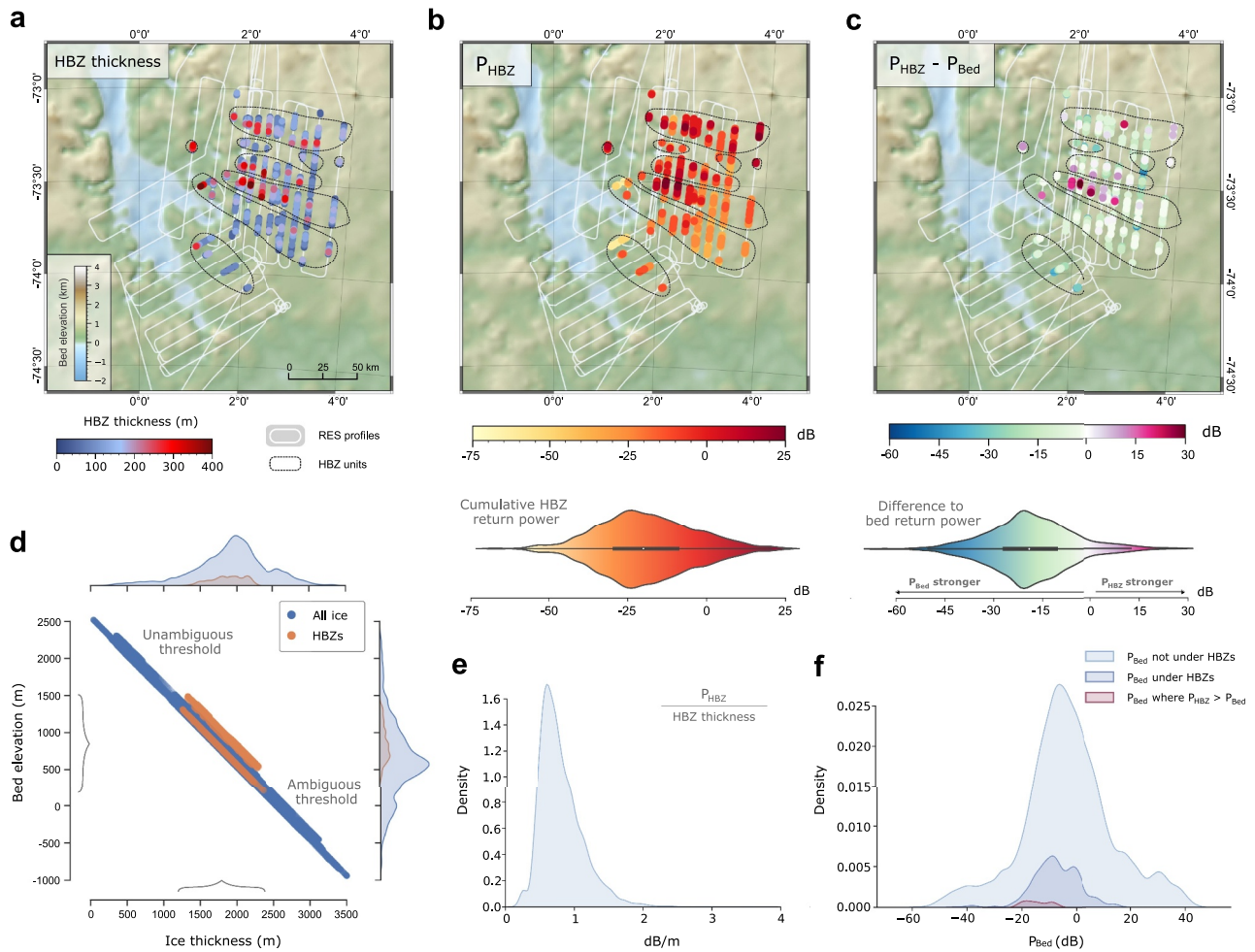
Figure 3. Spatial distribution of high-backscatter zone (HBZ) thickness and backscatter characteristics. (a) The thickness in meters of HBZs, (b) P_{HBZ}, and (c) $P_{HBZ}-P_{Bed}$. Values in (b), (c), and (e) were derived assuming a one-way englacial attenuation rate of 20 dB/km. HBZs along ice flow are grouped with a black polygon. Note that high values in (b) and (c) might appear disproportionately frequent, as higher values overlay the lower ones. Therefore, we show violin plots of the distribution of values underneath. The background map shows the bed topography (Morlighem et al., 2020). (d) The bed elevation versus ice thickness distribution for the entire data (blue) and the radar traces where an HBZ is present (orange). The respective abundance of ice thickness and bed elevation is shown as histograms on the top and right axes of (d). (e) Distribution of P_{HBZ} divided by HBZ thickness. (f) P_{Bed} for all locations where HBZs are not detected, for locations where HBZs were detected as well as for locations where $P_{HBZ} > P_{Bed}$.

In addition, we assess P_{Bed} at (a) locations where HBZs are not present, (b) locations where HBZs are present, and (c) locations where P_{HBZ} is stronger than P_{Bed} at the same location (Figure 3f). We defined particularly strong HBZs when the cumulative return power of the HBZs is larger compared to bed return power ($P_{HBZ} > P_{Bed}$). Notably, bed return power associated with HBZs exhibits a magnitude that is comparable to regions where HBZs are at a given ice thickness. However, in regions where HBZ are pronounced ($P_{HBZ} > P_{Bed}$), bed return power remains predominantly in the low-P_{Bed} regime at comparable ice thickness where HBZs were detected. This suggests that although HBZs can induce a quantifiable influence on P_{Bed}, they cause overall little radio-wave propagation loss.

3.3. Model Diagnosis of Bed Conditions for Possible Freeze-On

The results obtained from the thermomechanical model using GHF maps from Martos et al. (2017) and a range of constant GHF values reveal a distinctive spatial distribution of regions where either basal melting or basal freeze-on dominates (Figure 4a). Based on the overall modeling outputs considering the different GHF maps, we conclude that in the upstream parts of the catchment, basal temperatures are warm, and meltwater is generated
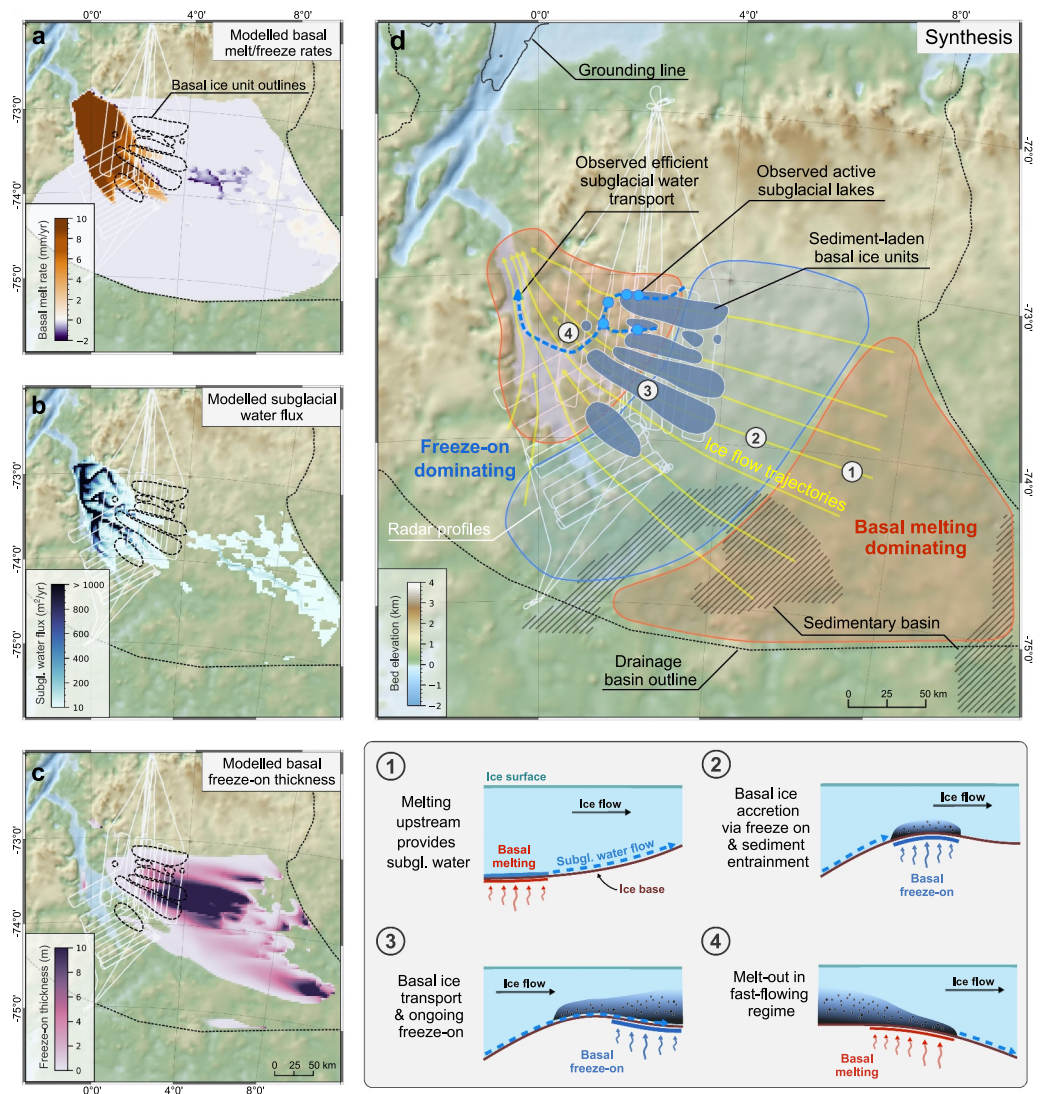
Figure 4. (a) Modeled basal melting, (b) subglacial water flux, and (c) modeled basal freeze-on thickness. All three model outputs were generated with the geothermal heat flux map by Martos et al. (2017) −15 mW/m². Panel (d) shows the synthesis of results highlighting the hypothesized spatial pattern where basal melting or freeze-on dominates. The numbers in (d) and the lower panel show the proposed mechanism to create the observed sediment-entrained basal ice units. Bed topography in panels (a)–(d) is from Morlighem et al. (2020), ice flow trajectories in (d) are based on the velocity field of Mouginot et al. (2019a), and subglacial lakes as well as channelized subglacial water propagation paths are from Neckel et al. (2021). Outlines of sedimentary basins upstream of our radar profiles in (d) are from Aitken et al. (2023).

because of thick ice and higher GHF values in the Martos et al. (2017) data set. This meltwater flows downstream toward the northwest, where it encounters thinner ice and potentially lower GHF values, triggering basal freeze-on (Figure 4b, and Figures S6–S8 and S10–S18 in Supporting Information S1). Further downstream, the ice base returns to basal melting conditions because of high levels of shear heating caused by rapid ice flow.

This pattern of warmer basal conditions in the upstream catchment, colder conditions in the middle near where the HBZs are observed, followed by warmer conditions further downstream, persists regardless of which GHF forcing we use (Figures S6–S8 and S10–S18 in Supporting Information S1). In cases where the mean GHF is low, this pattern is expressed in basal temperature, which is below freezing everywhere outside of the fast-flow ice stream but higher in the upstream catchment and lower in the middle region (Figure S8 in Supporting Information S1). When the mean GHF is higher, basal temperature reaches the melting point over a wider region,

10.1029/2023GL107164

however, some regions with basal freeze-on persist (Figure S8 in Supporting Information S1). For intermediate values of GHF, the "cold" portion of the warm-cold-warm pattern crosses over from basal melting to basal freezing, producing freeze-on units. This warm-cold-warm pattern is stronger using GHF forcing derived from Martos et al. (2017) because that data set has a drop of about 10 mW/m^2 from the upstream to the middle region (Figure S4 in Supporting Information S1). However, the pattern persists even with constant GHF forcing (Figure S8 in Supporting Information S1).

When comparing modeled freeze-on regions with different GHF maps to our mapped HBZs, we identify the following correlations. First, a significant portion of the predicted freeze-on regions align with our mapped HBZs in the northern section of our radar profiles. The extent and exact location depend on the chosen GHF. Moreover, model-predicted freezing extends further upstream from the mapped HBZs (Figure 4c and Figures S8 and S10–S18 in Supporting Information S1). However, in the downstream regions where HBZs are detected, the model often predicts basal melt rates and an absence of freeze-on. In the southern radar profile set, some of the models predict freeze-on despite the absence of radar-detected HBZs (Figure S5 in Supporting Information S1). We have not attempted to rigorously optimize GHF here, but we found that Martos −15 mW/m^2 is the best fit to our observations, producing freeze-on in the northern radar profile set but not the southern set (Figure S9 in Supporting Information S1).

4. Discussion

Prominent HBZs, characterized by their clear contrast to regions of ice with lower backscatter or echo-free characteristics, indicate variations of dielectric properties over a short vertical distance, pointing toward a region of heterogeneous material properties. The absence of clear reflection stratification indicates that point scatterers embedded within the ice are the most likely explanation for the observed reflection pattern. HBZ return power is too high and too continuous in range to be attributed to changes in ice crystal fabric (Lilien et al., 2021; Matsuoka et al., 2004). By contrast, owing to the low englacial attenuation observed within the HBZs, the presence of water droplets and, thus, temperate ice can be confidently ruled out (Franke et al., 2023; Ogier et al., 2023). Furthermore, electromagnetic forward modeling conducted at select prominent HBZs suggests embedded sediment with low dielectric properties (Franke et al., 2023). Considering measured particle concentrations in Antarctic ice within the range of ∼1%–20% (Christoffersen et al., 2010; Gow et al., 1979; Winter et al., 2019), we estimate a sediment volume of at least 1.8 km^3 within our study area (assuming the lower particle concentration boundary of 1%). This inference points toward the likely availability of a substantial amount of loose sediment within source regions where particles are embedded in the basal ice, which is supported by the potential location of sedimentary basins in the upstream region (Aitken et al., 2023).

Thermomechanical modeling provides insight into possible formation mechanisms of the basal ice units. The distribution of modeled rates of basal melting, freezing, and the thickness of freeze-on layers suggests that sediment-laden basal ice units likely formed through basal freeze-on. We hypothesize that basal melting upstream generates sufficient meltwater, which then refreezes as it flows downstream (Figure 4). Sediment suspended in the subglacial hydrological system is entrained into the ice column during the process of basal freeze-on, implying a net erosive effect as sediment is removed from the subglacial system and incorporated into the overlying ice sheet. It remains uncertain whether these basal ice units extend further upstream due to limitations in our radar data extent. Thus, our data cannot rule out the possibility that at least some of the basal ice units have been advected into our survey domain from an un-surveyed upstream freeze-on source region. However, the increase in thickness with distance downstream suggests that at least some of the freeze-on is being produced within our domain. In addition, our data do not constrain whether the basal freeze-on is a steady-state process or whether the basal hydrological system fluctuates in time.

It is evident from the modeling that the GHF should fall within a certain range, not too high to prevent basal freezing, yet not too low to hinder the production of subglacial water upstream. This pattern is strongest with the general spatial GHF distribution of Martos et al. (2017), as the upstream region exhibits a higher GHF compared to the area where we identified the basal ice. A uniform reduction of this GHF field by 5–15 mW/m^2 increases both the extent and thickness of modeled freeze-on ice, improving the fit with observations. However, basal freeze-on is still produced in our survey area, even with constant GHF, due to the reduction of ice thickness compared to the thicker upstream region. Yet even with the optimal modification, modeled freeze-on thickness is still an order of magnitude less than the observed thickness of the HBZs here (up to 350 m); hence, it is likely that

the observed basal ice units are subsequently thickening downstream as more mass is added to the ice base (Figure 4). Further increase of basal ice unit thickness could potentially be attributed to a non-steady state ice flow velocity field or other processes that can cause more complex deformation patterns, such as downstream migration of the freezing front (Wolovick & Creyts, 2016; Wolovick et al., 2014), rheological contrasts within the ice column (NEEM community members, 2013), or buckling due to convergent flow (Bons et al., 2016).

Overall, the detection of basal units is concentrated in the northern part of the radar profiles, even though some of our model runs also predict their presence in the southern part (Figure S8 in Supporting Information S1). One possible explanation for this discrepancy could be the availability of sediment. In the southern region, freeze-on may exist, but the accreted ice might not exhibit strong dielectric contrasts due to the lack of sediment for the entrainment process. However, this would contradict the location of sedimentary basins (Aitken et al., 2023) and findings where pure frozen ice at the base in other locations was documented (MacGregor et al., 2009). Still, sediment availability might also relate to the varying degrees of past erosion between the southern and northern survey region (Franke et al., 2021) leading to the hypothesis that unconsolidated sediment has been removed by past glacial flow in the southern region. Additionally, the availability of meltwater is a crucial factor. It is possible that meltwater may not be generated in the catchment area upstream of these regions, or that any meltwater generated in the upstream catchment is routed elsewhere. Alternatively, it is possible that basal units are produced upstream but thinned by ice flow or that the GHF is substantially higher here, such that the entire southern part of the survey area is melting at the base rather than freezing. However, sophisticated analyses of englacial attenuation, radar bed reflection and modeling would be necessary to better constrain the basal thermal state and thus allocate the presence of liquid water (Dawson et al., 2024; Schroeder et al., 2016).

5. Conclusion

The widespread distribution of high-backscatter units in the deepest part of the basal ice within the East Antarctic Jutulstraumen drainage basin has been revealed with high-resolution radar data. By analyzing their radar signature and combining these results with previous studies involving radar forward modeling and integrating three-dimensional thermomechanical modeling, we conclude that at these locations, the basal ice is composed of elongated three-dimensional ice complexes with entrained sediment, which have formed due to basal freeze-on of subglacial water and further amplified in thickness downstream. Notably, these basal ice units do not significantly contribute to the englacial attenuation of radar waves, implying that the embedded material exhibits comparable dielectric properties as the overlying ice what suggests a cold base. The emergence of these basal ice units is linked to the interplay between basal melting, basal freeze-on, subglacial water routing, and ice flow. Hence, basal ice units are only found at distinct locations within the Jutulstraumen catchment, primarily at the northern onset region of the Jutulstraumen glacier.

The presence of such basal ice units, which differ not only in dielectric but also in material properties, has the potential to significantly influence ice-sheet dynamics due to distinct and localized rheological properties. This is especially relevant for parameterizing ice flow and subglacial hydrology models. We suggest that the entrainment of sediment via basal freeze-on and subsequent transport via ice flow represents an important mechanism to consider regarding the cycle of materials in the ice-sheet system. Furthermore, the knowledge gained from this study promotes the use of these characteristic basal ice units as observationally-based markers for identifying instances of freezing and subglacial material entrainment and possibly constrain GHF. Consequently, this provides insights not only into the physical conditions at the ice base but also information about the presence of unconsolidated subglacial material, offering valuable insights into the underlying geology. Furthermore, our findings suggest that sediment-laden basal ice units may constitute a significant component of the AIS.

Data Availability Statement

Radar data products from the standard workflow of the JuRaS-2018 AWI UBW survey (Franke et al., 2023), HBZ locations and HBZ thickness (Franke & Wolovick, 2023), and outputs from the 3D thermomechanical modeling (Wolovick & Franke, 2023) are available on PANAEA. Furthermore, ice thickness data from the JuRaS-2018 AWI UWB radar survey (Franke et al., 2020) are available on PANGAEA, and are part of BEDMAP 3 (Frémand et al., 2023) and BedMachine Antarctica (Morlighem et al., 2020). Ice surface velocities (Mouginot

et al., 2019a) and drainage system boundaries (Mouginot et al., 2019b) are available at the National Snow and Ice Data Center.

References

Aitken, A. R. A., Li, L., Kulessa, B., Schroeder, D., Jordan, T. A., Whittaker, J. M., et al. (2023). Antarctic sedimentary basins and their influence on ice-sheet dynamics. *Reviews of Geophysics*, *61*(3), e2021RG000767. https://doi.org/10.1029/2021rg000767

Alfred-Wegener-Institut Helmholtz-Zentrum für Polar-und Meeresforschung. (2016). Polar aircraft Polar5 and Polar6 operated by the Alfred Wegener Institute. *Journal of Large-Scale Research Facilities JLSRF*, *2*, 87. https://doi.org/10.17815/jlsrf-2-153

Arthern, R. J., Winebrenner, D. P., & Vaughan, D. G. (2006). Antarctic snow accumulation mapped using polarization of 4.3-cm wavelength microwave emission. *Journal of Geophysical Research*, *111*(D6), D06107. https://doi.org/10.1029/2004jd005667

Bell, R. E., Ferraccioli, F., Creyts, T. T., Braaten, D., Corr, H., Das, I., et al. (2011). Widespread persistent thickening of the East Antarctic Ice Sheet by freezing from the base. *Science*, *331*(6024), 1592–1595. https://doi.org/10.1126/science.1200109

Bell, R. E., Tinto, K., Das, I., Wolovick, M., Chu, W., Creyts, T. T., et al. (2014). Deformation, warming and softening of Greenland's ice by refreezing meltwater. *Nature Geoscience*, *7*(7), 497–502. https://doi.org/10.1038/ngeo2179

Berg, W. V. D., Broeke, M. V. D., Reijmer, C., & Meijgaard, E. V. (2005). Characteristics of the Antarctic surface mass balance, 1958–2002, using a regional atmospheric climate model. *Annals of Glaciology*, *41*, 97–104. https://doi.org/10.3189/172756405781813302

Bons, P. D., Jansen, D., Mundel, F., Bauer, C. C., Binder, T., Eisen, O., et al. (2016). Converging flow and anisotropy cause large-scale folding in Greenland's ice sheet. *Nature Communications*, *7*(1), 11427. https://doi.org/10.1038/ncomms11427

Christoffersen, P., Tulaczyk, S., & Behar, A. (2010). Basal ice sequences in Antarctic ice stream: Exposure of past hydrologic conditions and a principal mode of sediment transfer. *Journal of Geophysical Research*, *115*(F3). https://doi.org/10.1029/2009jf001430

Comiso, J. C. (2000). Variability and trends in Antarctic surface temperatures from in situ and satellite infrared measurements. *Journal of Climate*, *13*(10), 1674–1696. https://doi.org/10.1175/1520-0442(2000)013⟨1674:vatias⟩2.0.co;2

Creyts, T. T., Ferraccioli, F., Bell, R. E., Wolovick, M., Corr, H., Rose, K. C., et al. (2014). Freezing of ridges and water networks preserves the Gamburtsev Subglacial Mountains for millions of years. *Geophysical Research Letters*, *41*(22), 8114–8122. https://doi.org/10.1002/2014gl061491

Dawson, E. J., Schroeder, D. M., Chu, W., Mantelli, E., & Seroussi, H. (2022). Ice mass loss sensitivity to the Antarctic ice sheet basal thermal state. *Nature Communications*, *13*(1), 4957. https://doi.org/10.1038/s41467-022-32632-2

Dawson, E. J., Schroeder, D. M., Chu, W., Mantelli, E., & Seroussi, H. (2024). Heterogeneous basal thermal conditions underpinning the Adélie-George V Coast, East Antarctica. *Geophysical Research Letters*, *51*(2), e2023GL105450. https://doi.org/10.1029/2023gl105450

Drews, R., Eisen, O., Weikusat, I., Kipfstuhl, S., Lambrecht, A., Steinhage, D., et al. (2009). Layer disturbances and the radio-echo free zone in ice sheets. *The Cryosphere*, *3*(2), 195–203. https://doi.org/10.5194/tc-3-195-2009

Franke, S., Eisermann, H., Jokat, W., Eagles, G., Asseng, J., Miller, H., et al. (2021). Preserved landscapes underneath the Antarctic Ice Sheet reveal the geomorphological history of Jutulstraumen Basin. *Earth Surface Processes and Landforms*, *46*(13), 2728–2745. https://doi.org/10.1002/esp.5203

Franke, S., Gerber, T., Warren, C., Jansen, D., Eisen, O., & Dahl-Jensen, D. (2023). Investigating the radar response of englacial debris entrained basal ice units in East Antarctica using electromagnetic forward modeling. *IEEE Transactions on Geoscience and Remote Sensing*, *61*, 1–16. https://doi.org/10.1109/tgrs.2023.3277874

Franke, S., Helm, V., Steinhage, D., & Jansen, D. (2023). Airborne radio-echo sounding data from Jutulstraumen Glacier (western Dronning Maud Land, East Antarctica) recorded with the AWI UWB radar system [Dataset]. PANGAEA. https://doi.org/10.1594/PANGAEA.962670

Franke, S., Jansen, D., Binder, T., Paden, J. D., Dörr, N., Gerber, T. A., et al. (2022). Airborne ultra-wideband radar sounding over the shear margins and along flow lines at the onset region of the Northeast Greenland Ice Stream. *Earth System Science Data*, *14*(2), 763–779. https://doi.org/10.5194/essd-14-763-2022

Franke, S., Jansen, D., & Helm, V. (2020). Ice Thickness from Jutulstraumen Glacier recorded with the airborne AWI UWB radar system, Antarctica [Dataset]. PANGAEA. https://doi.org/10.1594/PANGAEA.911475

Franke, S., & Wolovick, M. (2023). Locations and thickness of sediment-laden basal ice zones at Jutulstraumen Glacier onset (East Antarctica) [Dataset]. PANGAEA. https://doi.org/10.1594/PANGAEA.963889

Frémand, A. C., Fretwell, P., Bodart, J. A., Pritchard, H. D., Aitken, A., Bamber, J. L., et al. (2023). Antarctic Bedmap data: Findable, Accessible, Interoperable, and Reusable (FAIR) sharing of 60 years of ice bed, surface, and thickness data. *Earth System Science Data*, *15*(7), 2695–2710. https://doi.org/10.5194/essd-15-2695-2023

Gades, A., Raymond, C., Conway, H., & Jacobel, R. (2000). Bed properties of Siple Dome and adjacent ice streams, West Antarctica, inferred from radio-echo sounding measurements. *Journal of Glaciology*, *46*(152), 88–94. https://doi.org/10.3189/172756500781833467

Garbe, J., Albrecht, T., Levermann, A., Donges, J. F., & Winkelmann, R. (2020). The hysteresis of the Antarctic ice sheet. *Nature*, *585*(7826), 538–544. https://doi.org/10.1038/s41586-020-2727-5

Gow, A. J., Epstein, S., & Sheehy, W. (1979). On the origin of stratified debris in ice cores from the bottom of the Antarctic ice sheet. *Journal of Glaciology*, *23*(89), 185–192. https://doi.org/10.3189/s0022143000029828

Jordan, T. M., Bamber, J. L., Williams, C. N., Paden, J. D., Siegert, M. J., Huybrechts, P., et al. (2016). An ice-sheet-wide framework for englacial attenuation from ice-penetrating radar data. *The Cryosphere*, *10*(4), 1547–1570. https://doi.org/10.5194/tc-10-1547-2016

Kang, H., Zhao, L., Wolovick, M., & Moore, J. C. (2022). Evaluation of six geothermal heat flux maps for the antarctic lambert–amery glacial system. *The Cryosphere*, *16*(9), 3619–3633. https://doi.org/10.5194/tc-16-3619-2022

Karlsson, N. B., Binder, T., Eagles, G., Helm, V., Pattyn, F., Liefferinge, B. V., & Eisen, O. (2018). Glaciological characteristics in the Dome Fuji region and new assessment for "Oldest Ice". *The Cryosphere*, *12*(7), 2413–2424. https://doi.org/10.5194/tc-12-2413-2018

Kazmierczak, E., Sun, S., Coulon, V., & Pattyn, F. (2022). Subglacial hydrology modulates basal sliding response of the Antarctic ice sheet to climate forcing. *The Cryosphere*, *16*(10), 4537–4552. https://doi.org/10.5194/tc-16-4537-2022

Kjær, K. H., Larsen, N. K., Binder, T., Bjørk, A. A., Eisen, O., Fahnestock, M. A., et al. (2018). A large impact crater beneath Hiawatha Glacier in northwest Greenland. *Science Advances*, *4*(11), eaar8173. https://doi.org/10.1126/sciadv.aar8173

Le Brocq, A. M., Payne, A. J., & Vieli, A. (2010). An improved Antarctic dataset for high resolution numerical ice sheet models (ALBMAP v1). *Earth System Science Data*, *2*(2), 247–260. https://doi.org/10.5194/essd-2-247-2010

Leysinger Vieli, G. J.-M. C., Martín, C., Hindmarsh, R. C. A., & Lüthi, M. P. (2018). Basal freeze-on generates complex ice-sheet stratigraphy. *Nature Communications*, *9*(1), 4669. https://doi.org/10.1038/s41467-018-07083-3

Lilien, D. A., Steinhage, D., Taylor, D., Parrenin, F., Ritz, C., Mulvaney, R., et al. (2021). Brief communication: New radar constraints support presence of ice older than 1.5 Myr at Little Dome C. *The Cryosphere*, *15*(4), 1881–1888. https://doi.org/10.5194/tc-15-1881-2021

MacGregor, J., Matsuoka, K., & Studinger, M. (2009). Radar detection of accreted ice over Lake Vostok, Antarctica. *Earth and Planetary Science Letters*, *282*(1–4), 222–233. https://doi.org/10.1016/j.epsl.2009.03.018

Martos, Y. M., Catalán, M., Jordan, T. A., Golynsky, A., Golynsky, D., Eagles, G., & Vaughan, D. G. (2017). Heat flux distribution of Antarctica unveiled. *Geophysical Research Letters*, *44*(22), 11417–11426. https://doi.org/10.1002/2017gl075609

Matsuoka, K., MacGregor, J. A., & Pattyn, F. (2012). Predicting radar attenuation within the Antarctic ice sheet. *Earth and Planetary Science Letters*, *359*, 173–183. https://doi.org/10.1016/j.epsl.2012.10.018

Matsuoka, K., Uratsuka, S., Fujita, S., & Nishio, F. (2004). Ice-flow-induced scattering zone within the Antarctic ice sheet revealed by high-frequency airborne radar. *Journal of Glaciology*, *50*(170), 382–388. https://doi.org/10.3189/172756504781829891

Morlighem, M., Rignot, E., Binder, T., Blankenship, D., Drews, R., Eagles, G., et al. (2020). Deep glacial troughs and stabilizing ridges unveiled beneath the margins of the Antarctic ice sheet. *Nature Geoscience*, *13*(2), 132–137. https://doi.org/10.1038/s41561-019-0510-8

Mouginot, J., Rignot, E., & Scheuchl, B. (2019a). Continent-wide, interferometric SAR phase, mapping of Antarctic ice velocity. *Geophysical Research Letters*, *46*(16), 9710–9718. https://doi.org/10.1029/2019gl083826

Mouginot, J., Rignot, E., & Scheuchl, B. (2019b). Phase-based Antarctica ice velocity map [Dataset]. Dryad. https://doi.org/10.7280/D10D4Z

Neckel, N., Franke, S., Helm, V., Drews, R., & Jansen, D. (2021). Evidence of cascading subglacial water flow at Jutulstraumen Glacier (Antarctica) derived from Sentinel-1 and ICESat-2 measurements. *Geophysical Research Letters*, *48*(20), e2021GL094472. https://doi.org/10.1029/2021gl094472

NEEM community members. (2013). Eemian interglacial reconstructed from a Greenland folded ice core. *Nature*, *493*(7433), 489–494. https://doi.org/10.1038/nature11789

Nixdorf, U., Steinhage, D., Meyer, U., Hempel, L., Jenett, M., Wachs, P., & Miller, H. (1999). The newly developed airborne radio-echo sounding system of the AWI as a glaciological tool. *Annals of Glaciology*, *29*, 231–238. https://doi.org/10.3189/172756499781821346

Ogier, C., Manen, D.-J. V., Maurer, H., Räss, L., Hertrich, M., Bauder, A., & Farinotti, D. (2023). Ground penetrating radar in temperate ice: Englacial water inclusions as limiting factor for data interpretation. *Journal of Glaciology*, 1–12. https://doi.org/10.1017/jog.2023.68

Oswald, G., & Gogineni, S. (2008). Recovery of subglacial water extent from Greenland radar survey data. *Journal of Glaciology*, *54*(184), 94–106. https://doi.org/10.3189/002214308784409107

Pattyn, F. (2010). Antarctic subglacial conditions inferred from a hybrid ice sheet/ice stream model. *Earth and Planetary Science Letters*, *295*(3–4), 451–461. https://doi.org/10.1016/j.epsl.2010.04.025

Pollard, D., & DeConto, R. M. (2012). A simple inverse method for the distribution of basal sliding coefficients under ice sheets, applied to Antarctica. *The Cryosphere*, *6*(5), 953–971. https://doi.org/10.5194/tc-6-953-2012

Robin, G. D. Q., Evans, S., & Bailey, J. T. (1969). Interpretation of radio echo sounding in polar ice sheets. *Philosophical Transactions of the Royal Society of London. Series A, Mathematical and Physical Sciences*, *265*(1166), 437–505. https://doi.org/10.1098/rsta.1969.0063

Rodriguez-Morales, F., Byers, K., Crowe, R., Player, K., Hale, R. D., Arnold, E. J., et al. (2013). Advanced multifrequency radar instrumentation for polar research. *IEEE Transactions on Geoscience and Remote Sensing*, *52*(5), 2824–2842. https://doi.org/10.1109/tgrs.2013.2266415

Ross, N., Corr, H., & Siegert, M. (2020). Large-scale englacial folding and deep-ice stratigraphy within the West Antarctic Ice Sheet. *The Cryosphere*, *14*(6), 2103–2114. https://doi.org/10.5194/tc-14-2103-2020

Schroeder, D. M., Blankenship, D. D., & Young, D. A. (2013). Evidence for a water system transition beneath Thwaites Glacier, West Antarctica. *Proceedings of the National Academy of Sciences*, *110*(30), 12225–12228. https://doi.org/10.1073/pnas.1302828110

Schroeder, D. M., Seroussi, H., Chu, W., & Young, D. A. (2016). Adaptively constraining radar attenuation and temperature across the Thwaites Glacier catchment using bed echoes. *Journal of Glaciology*, *62*(236), 1075–1082. https://doi.org/10.1017/jog.2016.100

Stokes, C. R., Abram, N. J., Bentley, M. J., Edwards, T. L., England, M. H., Foppert, A., et al. (2022). Response of the East Antarctic Ice Sheet to past and future climate change. *Nature*, *608*(7922), 275–286. https://doi.org/10.1038/s41586-022-04946-0

Wang, Z., Chung, A., Steinhage, D., Parrenin, F., Freitag, J., & Eisen, O. (2023). Mapping age and basal conditions of ice in the Dome Fuji region, Antarctica, by combining radar internal layer stratigraphy and flow modeling. *The Cryosphere*, *17*(10), 4297–4314. https://doi.org/10.5194/tc-17-4297-2023

Winter, K., Woodward, J., Ross, N., Dunning, S. A., Hein, A. S., Westoby, M. J., et al. (2019). Radar-detected englacial debris in the West Antarctic Ice Sheet. *Geophysical Research Letters*, *46*(17–18), 10454–10462. https://doi.org/10.1029/2019gl084012

Wolovick, M., & Franke, S. (2023). Modeled freeze-on rates at Jutulstraumen Glacier onset (East Antarctica) [Dataset]. PANGAEA. https://doi.org/10.1594/PANGAEA.963891

Wolovick, M. J., & Creyts, T. T. (2016). Overturned folds in ice sheets: Insights from a kinematic model of traveling sticky patches and comparisons with observations. *Journal of Geophysical Research: Earth Surface*, *121*(5), 1065–1083. https://doi.org/10.1002/2015JF003698

Wolovick, M. J., Creyts, T. T., Buck, W. R., & Bell, R. E. (2014). Traveling slippery patches produce thickness-scale folds in ice sheets. *Geophysical Research Letters*, *41*(24), 8895–8901. https://doi.org/10.1002/2014gl062248

Wolovick, M. J., Moore, J. C., & Zhao, L. (2021). Joint inversion for surface accumulation rate and geothermal heat flow from ice-penetrating radar observations at Dome A, East Antarctica. Part I: Model description, data constraints, and inversion results. *Journal of Geophysical Research: Earth Surface*, *126*(5), e2020JF005937. https://doi.org/10.1029/2020JF005937

Wrona, T., Wolovick, M. J., Ferraccioli, F., Corr, H., Jordan, T., & Siegert, M. J. (2018). Position and variability of complex structures in the central East Antarctic Ice Sheet. *Special Publications*, *461*(1), 113–129. https://doi.org/10.1144/sp461.12

References From the Supporting Information

An, M., Wiens, D. A., Zhao, Y., Feng, M., Nyblade, A., Kanao, M., et al. (2015). Temperature, lithosphere-asthenosphere boundary, and heat flux beneath the Antarctic Plate inferred from seismic velocities. *Journal of Geophysical Research: Solid Earth*, *120*(12), 8720–8742. https://doi.org/10.1002/2015jb011917

Franke, S., Jansen, D., Beyer, S., Neckel, N., Binder, T., Paden, J., & Eisen, O. (2021). Complex basal conditions and their influence on ice flow at the onset of the Northeast Greenland ice stream. *Journal of Geophysical Research: Earth Surface*, *126*(3), e2020JF005689. https://doi.org/10.1029/2020jf005689

Haeger, C., Petrunin, A. G., & Kaban, M. K. (2022). Geothermal heat flow and thermal structure of the Antarctic lithosphere. *Geochemistry, Geophysics, Geosystems*, *23*(10), e2022GC010501. https://doi.org/10.1029/2022gc010501

Lösing, M., & Ebbing, J. (2021). Predicting geothermal heat flow in Antarctica with a machine learning approach. *Journal of Geophysical Research: Solid Earth*, *126*(6), e2020JB021499. https://doi.org/10.1029/2020jb021499

Purucker, M. (2012). Geothermal heat flux data set based on low resolution observations collected by the CHAMP satellite between 2000 and 2010, and produced from the MF-6 model following the technique described in Fox Maule et al. (2005) [Dataset]. http://websrv.cs.umt.edu/isis/images/c/c8/Antarctica_heat_flux_5km.nc

Shapiro, N. M., & Ritzwoller, M. H. (2004). Inferring surface heat flux distributions guided by a global seismic model: Particular application to Antarctica. *Earth and Planetary Science Letters*, *223*(1–2), 213–224. https://doi.org/10.1016/j.epsl.2004.04.011

Shen, W., Wiens, D. A., Lloyd, A. J., & Nyblade, A. A. (2020). A geothermal heat flux map of Antarctica empirically constrained by seismic structure. *Geophysical Research Letters*, *47*(14). https://doi.org/10.1029/2020gl086955

Stål, T., Reading, A. M., Halpin, J. A., & Whittaker, J. M. (2021). Antarctic geothermal heat flow model: Aq1. *Geochemistry, Geophysics, Geosystems*, *22*(2), e2020GC009428. https://doi.org/10.1029/2020gc009428